Magnon excitation and spin-phonon coupling in $A_2Ir_2O_7$ (A = Gd, Dy, and Er)

M. Rosalin,[1] Prachi Telang,[2] Surjeet Singh,[2] D. V. S. Muthu,[1] and A. K. Sood[1,*]

[1]*Department of Physics, Indian Institute of Science, Bangalore 560012, India*

[2]*Department of Physics, Indian Institute of Science Education and Research, Pune, Maharashtra 411008, India*

(Received 3 March 2024; revised 18 April 2024; accepted 8 May 2024; published 21 May 2024)

We present a comparative study of the temperature-dependent Raman scattering of pyrochlore iridates $A_2Ir_2O_7$, where A = Gd, Dy, and Er, spanning the temperature range from 295 to 5 K. Our investigation covers the metal-insulator phase transition, coinciding with the paramagnetic-to-all-in/all-out (AIAO) spin ordering at the magnetic transition temperature T_N. The crystal symmetry remains unchanged across this magnetic transition. Below T_N, two additional modes (N_1 and N_2) emerge, associated with single magnon excitations within the AIAO-ordered state. Analysis of magnon energies enables us to estimate the isotropic exchange (J) and Dzyaloshinskii-Moriya interaction parameter (D). The resulting D/J ratios are ~0.15 for $Gd_2Ir_2O_7$ and $Dy_2Ir_2O_7$. In all the three systems, the Ir-O-Ir bond bending vibrations, A_{1g} and E_g, exhibit anomalous frequency softening in the magnetically ordered AIAO state, primarily originating from the spin-phonon interaction induced by the phonon modulation of the Dzyaloshinskii-Moriya spin-exchange interaction. The two stretching modes T_{2g}^2 and T_{2g}^4 experience significant hardening in the magnetic insulating phase. Additionally, substantial anomalous linewidth broadening of the E_g mode is observed in all samples, indicating strong phonon renormalization below T_N. Our experimental findings establish experimental evidence of magnon excitations and strong spin-phonon coupling in the AIAO-ordered state for these iridates.

DOI: 10.1103/PhysRevB.109.184434

I. INTRODUCTION

The study of strongly correlated electron systems over the years has yielded profound insights into the fundamental physics underlying emergent phases of matter. Among these systems, pyrochlore iridates have emerged as a prominent and intriguing class of materials due to their intricate interplay of various physical phenomena. These compounds $A_2Ir_2O_7$, where A represents a rare-earth or alkaline-earth metal (Pr to Lu, Bi or Y) belong to the pyrochlore oxide family. Strong spin-orbit coupling (SOC) and intermediate electron correlations allow this family of iridates to display a variety of topological phases, including topological Mott insulator and Weyl semimetal (WSM) [1,2] along with unique characteristics that may find application in magnetotransport and spintronics [3–5]. The crystal structure comprises a three-dimensional corner-sharing tetrahedra network hosting iridium ions with pronounced spin-orbit coupling and electron-electron correlations [6]. This unique combination of structural arrangement and electronic properties leads to making them an ideal platform for exploring novel quantum states [1,2,4,7,8]. For A = Pr, $A_2Ir_2O_7$ is metallic; A = Sm, Eu, and Nd is semimetallic; and for A = Gd, Tb, Dy, Ho, and Er, $A_2Ir_2O_7$ is semiconducting [9–13]. The low-temperature ground state of $A_2Ir_2O_7$ changes from a nonmagnetic metal for A = Pr and Bi to an antiferromagnetic insulator for A = Gd, Tb, Dy to Lu, and Y. The intermediate A = Nd, Sm, and Eu members, on the other hand, exhibit a temperature-induced metal-to-insulator transition (MIT) at T_N, which coincides with the antiferromagnetic (AFM) ordering of Ir^{4+} moments in an all-in, all-out (AIAO) structure (see Fig. S1 [14]) [10]. Remarkably, this ordering phenomenon manifests consistently across all iridates, irrespective of the magnetism of the A-site cation, defining the significance of Ir^{4+} ($J_{\text{eff}} = 1/2$) sublattice ordering as the primary source of magnetism in pyrochlore iridates. Additionally, in certain iridates with magnetic A-site element, A-sublattice undergoes AIAO magnetic ordering at significantly lower temperatures, below 10–15 K [15]. Although the conductivity of $A_2Ir_2O_7$ for A = Gd, Tb, Dy, Ho, and Er is semiconducting like with a small energy gap at ambient temperature, MIT is adopted because a common feature [a continuous increase of ρ (T) below T_N (T_{MI}) without saturation on cooling] in their transition is observed [12,16,17]. The electrical conductivity of $A_2Ir_2O_7$ tends to depend on the ionic radius of A and T_N increases with decreasing ionic radius [12,18]. Since the A ion is trivalent, the $(5d)^5$ electrons from Ir^{4+} form an unfilled t_{2g} band and contribute to the electrical conductivity. The most important consequence of the A substitution is the change of oxygen coordinates, which results in a slightly different Ir hybridization and effective Ir-t_{2g} bandwidth. The Ir-O-Ir bond angle reduces as the ionic radius of A decreases, narrowing the t_{2g} bandwidth [10].

In recent years, the role of spin-phonon coupling (SPC) in transition metal oxides has been recognized to be important in understanding the phase behavior of these compounds through observations of phenomena such as the thermal Hall effect [19], magnetic order stabilization with epitaxial strain [20], multiferroics and spintronics [21–24]. Even in

*asood@iisc.ac.in

the absence of any structural transition across T_N or T_{MI}, Raman and infrared studies on some of the pyrochlore iridates show phonon anomalies at and below T_N. In this context, our previous studies of optical phonons in $Pr_2Ir_2O_7$ [25] and Bi-doped $Eu_2Ir_2O_7$ [26] and $Sm_2Ir_2O_7$ [27] have shown anomalous temperature dependence of phonons associated with phonon-phonon, electron-phonon, and spin-phonon interactions. We have also observed signatures of strong spin-spin and electronic correlations in these compounds. In the present comparative study, we search for these distinct characteristics focusing on AIAO transition concerning the A-cation radius in the insulating states of three specific pyrochlore compounds: $Gd_2Ir_2O_7$, $Dy_2Ir_2O_7$, and $Er_2Ir_2O_7$. These compounds have garnered significant attention for their diverse magnetic ground states, stemming from the interplay between rare earth ions and iridium atoms within their crystal structures. Pyrochlore iridates are excellent candidates for showing topological magnon bands and robust spin-phonon coupling, as suggested theoretically [28]. However, there are not many experimental reports to support this. Motivated by this, we have done a detailed temperature-dependent Raman investigation of $A_2Ir_2O_7$, where A = Gd, Dy, and Er spanning the temperature range from 295 to 5 K and focusing on the phonon behavior in the low-temperature magnetic phase. We show that two additional modes (N_1 and N_2) emerge below T_N, and are associated with single magnon excitations within the AIAO-ordered state. We can estimate the isotropic exchange (J) and Dzyaloshinskii-Moriya interaction parameter (D) by analyzing magnon energies. This leads to D/J ratios of ~0.15 for $Gd_2Ir_2O_7$ and $Dy_2Ir_2O_7$, not estimated in earlier studies. The Ir-O-Ir bond bending vibrations with A_{1g} and E_g irreducible representation exhibit anomalous frequency softening in the magnetically ordered AIAO state. This softening primarily stems from the spin-phonon interaction induced by the phonon modulation of the Dzyaloshinskii-Moriya spin-exchange interaction. Additionally, a significant anomalous linewidth broadening of the E_g mode is observed below T_N. Furthermore, the two stretching modes T_{2g}^2 and T_{2g}^4 experience notable hardening in the magnetic insulating phase. The T_{2g}^1 phonon demonstrates pronounced linewidth broadening above T_N, possibly due to electron-phonon coupling.

II. EXPERIMENTAL DETAILS

High-quality polycrystalline samples of $Gd_2Ir_2O_7$ and $Dy_2Ir_2O_7$ were prepared using the standard solid-state reaction using high-purity (>99.9 %) precursors. The precursors for $Dy_2Ir_2O_7$ were Dy_2O_3 (Alfa aesar, 99.9%) and IrO_2 (Sigma Aldrich, 99.9%), and for the $Gd_2Ir_2O_7$ were Gd_2O_3 (Sigma Aldrich, 99.9%) and IrO_2 (Alfa aesar, 99.9%). The $Er_2Ir_2O_7$ was synthesized using a wet chemical reaction method in a single sintering step at T = 1273 K (at temperature well below the sublimation point of IrO_2) (see [29] for details). The phase formation was monitored using a Bruker D8 Advance powder x-ray diffractometer. The oxidation states of the elements were characterized by x-ray photoelectron spectroscopy (XPS) using a thermo-scientific K-ALPHA, Surface analysis system equipped with a monochromatic Al source (Kα = 1486.6 eV). The values of T_N for Gd, Dy, and Er iridates are 123, 130, (see chapter 6 in [30]) and 137 K [29], respectively, compared favorably with literature values (see Fig. S1 [14]) [11,12,16,31,32]. The unpolarized Raman spectra were recorded in backscattering geometry using HORIBA LabRAM HR Evolution Spectrometer and Peltier-cooled CCD detector (Jobin Yvon, Syncerity). The excitation wavelength of the laser was 532 nm, and the laser power was minimized to <0.3 mW to avoid any local heating of the sample. The low-temperature Raman measurements (5 to 295 K) were performed using closed-cycle He-cryostat, Cryostation S50, Montana. The recorded Raman spectra were fitted with Lorentzian functions to extract the frequency and linewidth [full width at half maximum (FWHM)] of individual Raman modes, and the error bars on the frequencies and linewidth values are obtained through nonlinear least square fitting of data using the ORIGIN software package [33].

III. RESULTS AND DISCUSSIONS

A. Structural characterization

The compounds of stoichiometry $A_2B_2O_7$ crystallize with the pyrochlore structure if the ratio of ionic radii of the cations A^{3+} and B^{4+} falls within the "pyrochlore stability field," defined as $1.46 < r_{A^{3+}}/r_{B^{4+}} < 1.80$. $A_2Ir_2O_7$, or more precisely, $A_2Ir_2O_6O'$, is an iridate from the pyrochlore family that crystallizes in the cubic space group $Fd\bar{3}m$ (z = 8) with A^{3+} at Wyckoff positions 16d (0.5, 0.5, 0.5), Ir^{4+} at 16c (0, 0, 0), O and O′ at 48f (x, 0.125, 0.125), and 8b (0.375, 0.375, 0.375), respectively [34]. In parallel with the body diagonals of the cubic unit cell, both A and Ir form interpenetrating corner-shared tetrahedral networks where the two sublattices are displaced relative to one another along the unit cell edge by length $a/2$, a being the lattice parameter. In contrast to A cation, which is in eightfold environment surrounded by six O and two O′ ions, the Ir ion coordinates with six O ions to create an IrO_6 octahedron. The ideal octahedral symmetry is achieved for x = 0.3125 within the field of stability of the pyrochlore structure, i.e., $0.3125 \leqslant x \leqslant 0.375$. In most known pyrochlores, the value of x lies well within these limits, and the IrO_6 octahedral exhibits a trigonal compression with increasing x. In the pyrochlore iridates, the typical value of x is estimated to be around 0.333, and the corresponding value of the bond angle Ir-O-Ir increases, consequently increasing the electronic bandwidth with varying A-site [35].

Figure 1 shows room temperature XRD patterns and Rietveld refinement results for $Gd_2Ir_2O_7$ and $Dy_2Ir_2O_7$. We performed a single-phase refinement for $Dy_2Ir_2O_7$ and a mixed-phase refinement for $Gd_2Ir_2O_7$ using the Fullprof suite. The Rietveld refinements demonstrated that all samples crystallize in the cubic $Fd\bar{3}m$ space group, showcasing predominantly pure phases with only a few Ir metal impurity peaks in the case of $Gd_2Ir_2O_7$. These impurity peaks, attributed to the volatility of IrO_2 at high temperatures, are illustrated in Fig. 1. The lattice constants extracted from the Rietveld refinement were 10.28 and 10.22 Å for $Gd_2Ir_2O_7$ and $Dy_2Ir_2O_7$, respectively. The Rietveld refinement parameters for $Gd_2Ir_2O_7$ and $Dy_2Ir_2O_7$ are plotted in Fig. S2 [14] along with other iridates, values taken from previous studies from our group [25,26,36]. It is shown by Zhang *et al.* that the Ir-O bond length and the Ir-O-Ir bond angle are closely

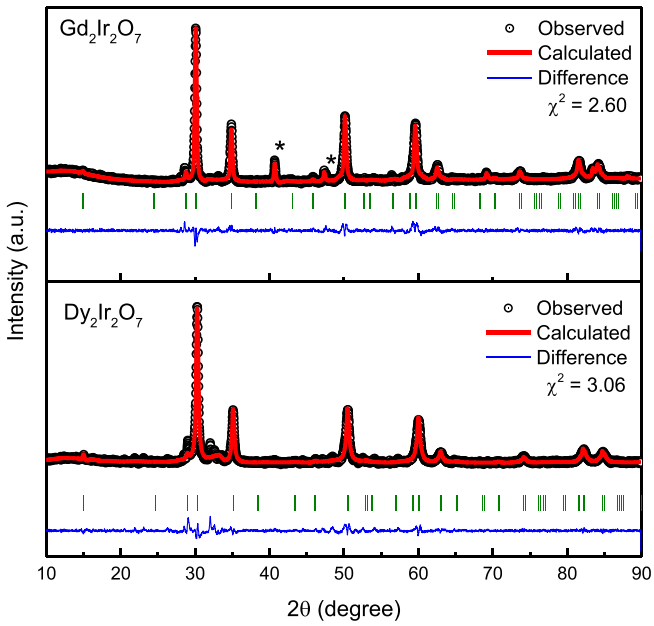

FIG. 1. Powder XRD pattern of $Gd_2Ir_2O_7$ and $Dy_2Ir_2O_7$ at 300 K at the top and bottom panel, respectively. Green bars indicate Bragg peaks, and the star symbol in the top panel marks the Ir metal impurity peaks in $Gd_2Ir_2O_7$. The XRD pattern for $Er_2Ir_2O_7$ is given in Ref. [29].

correlated with the t_{2g}-electronic bandwidth and the average hybridization function, and its variation is determined by the change of the 48f oxygen coordinate (x) by varying the A-site cation [10]. In an instance where two corner-sharing IrO_6 octahedra have two IrO_4 plaquettes on the same plane, an Ir-O-Ir bond angle of 180 ° would favor electrons hopping between two Ir atoms via the oxygen atom in between. Hence, a bending of Ir-O-Ir bond angle results in smaller electron hopping parameters between Ir atoms and leads to a smaller bandwidth. However, a shorter Ir-O distance may promote the hybridization of the Ir-5d and O-2p orbitals, increasing hopping and, thus, bandwidth. Typically, for a solid composed of corner-sharing IrO_6 octahedra, the t_{2g} orbitals of adjacent Ir atoms can interact with π-type orbitals via the Ir-O-Ir bridges. These interactions are strengthened by increasing the Ir-O-Ir angle and shortening the Ir-O bond, which increases the total width of the t_{2g}-block bands [10,37]. Hence, increasing the A-site atomic radius in $A_2Ir_2O_7$ increases the Ir-O-Ir bond angle and the lattice parameter in parallel and shortens the Ir-O bond length [10,37–39]. This is true for all rare earth iridates (for A = Gd to Pr) in this study, as shown in Fig. S2 [14]. However, $Dy_2Ir_2O_7$ does not fall into this lattice parameter trend but rather varies consistently with the oxygen parameter (x). Instead of its semiconducting nature, $Dy_2Ir_2O_7$ shows a larger Ir-O-Ir bond angle and smaller Ir-O bond length compared to $A_2Ir_2O_7$ (A = Gd, Eu, and Sm) similar to previous studies [40,41]. It should be noted that the bond length and bond angle values obtained for all the iridates in this study are in good agreement with earlier reports [40–42]. Hence, the internal oxygen coordinate is the most important structural parameter in determining the Ir-O bond length and Ir-O-Ir bond angle in $A_2Ir_2O_7$. The oxidation state of the iridium ion was determined using x-ray photoemission spectroscopy (XPS) studies (see Fig. S3 [14]). The carbon 1s peak with a binding energy (BE) of 284.8 eV was used to calibrate the observed XPS spectra. The Ir-4f core-level spectra were analyzed using the standard CasaXPS software suite, as shown in Figs. S3(a) and S3(b). The Shirley function was used to define the background. The Gaussian-Lorentz peak profile function was used to deconvolute the spectra. The photoemission spectra of Ir-based compounds are characterized by a pair of spin-orbit split doublets (I and II), identified as screened (II) and unscreened doublets (I) of Ir-core level [43,44]. The binding energies from the fitting for the narrow and intense doublet II, in this case, are found to be 65.6 and 62.5 eV in both the cases of $Gd_2Ir_2O_7$ and $Dy_2Ir_2O_7$, respectively, for $4f_{7/2}$ and $4f_{5/2}$ states. The spin-orbit splitting between $4f_{5/2}$ and $4f_{7/2}$ is found to be 3.1 eV, which agrees well with previously published values [43,45,46].

B. Ambient Raman spectra

Figure 2(a) shows Raman spectra of $A_2Ir_2O_7$ for A = Gd, Dy, and Er (this study), along with A = Pr, Sm, and Eu from recent studies of our group [25–27] for comparison. The spectra are characterized by the presence of six Raman-active phonon modes labeled T_{2g}^1, E_g, T_{2g}^2, A_{1g}, T_{2g}^3 and T_{2g}^4 as per the factor group analysis of the Raman-active phonon modes for the pyrochlore lattice [47]. Since the A and Ir sites have centers of symmetry, the observed vibrations involve only O and O′ atoms. The E_g and A_{1g} modes are related to the Ir-O-Ir bending while the first two T_{2g} (T_{2g}^1 and T_{2g}^2) are A-O stretching, and T_{2g}^4 mode is associated with the Ir-O stretching, respectively. Notably, the highest frequency is associated with Ir-O bond stretching due to its involvement in the vibration of the shortest bonds [48]. The phonon eigenmodes have been assigned based on the largest displacement of oxygen ions [49]. The weak T_{2g}^3 mode refers to the vibration of O′ surrounded by eight A ions [47]. The shoulders on the high energy side of T_{2g}^4 for all the iridates have been identified as second-order Raman modes [48,50]. All the phonon modes soften significantly with increasing ionic radius of the A-site cation, as shown in Fig. 2(b). The highest shift is found in the case of T_{2g}^4 (∼62 cm^{-1}), although the other modes also vary significantly, T_{2g}^1 and T_{2g}^2 by ∼25 and 17 cm^{-1}, and E_g and A_{1g} by ∼20 and 14 cm^{-1}, respectively. These trends are due to the modification of the A-O and Ir-O bond lengths as well as the Ir-O-Ir bond angle with different rare earth substitutions at the A site. Figure 2(b) illustrates a monotonic change in phonon frequencies regardless of variations in the Ir-O-Ir angle and Ir-O bond length [see Figs. S2(c) and S2(d)] [14]. However, this trend is consistent with the variation of the lattice parameter as a function of the ionic radius of A site cation as shown in Fig. S2(a) [14].

C. Temperature-dependent studies

Temperature-dependent Raman spectra of $Gd_2Ir_2O_7$, $Dy_2Ir_2O_7$, and $Er_2Ir_2O_7$ were recorded at different temperatures as shown in Figs. S4(a)– S4(c) [14]. The individual contributions of different phonon modes are determined by

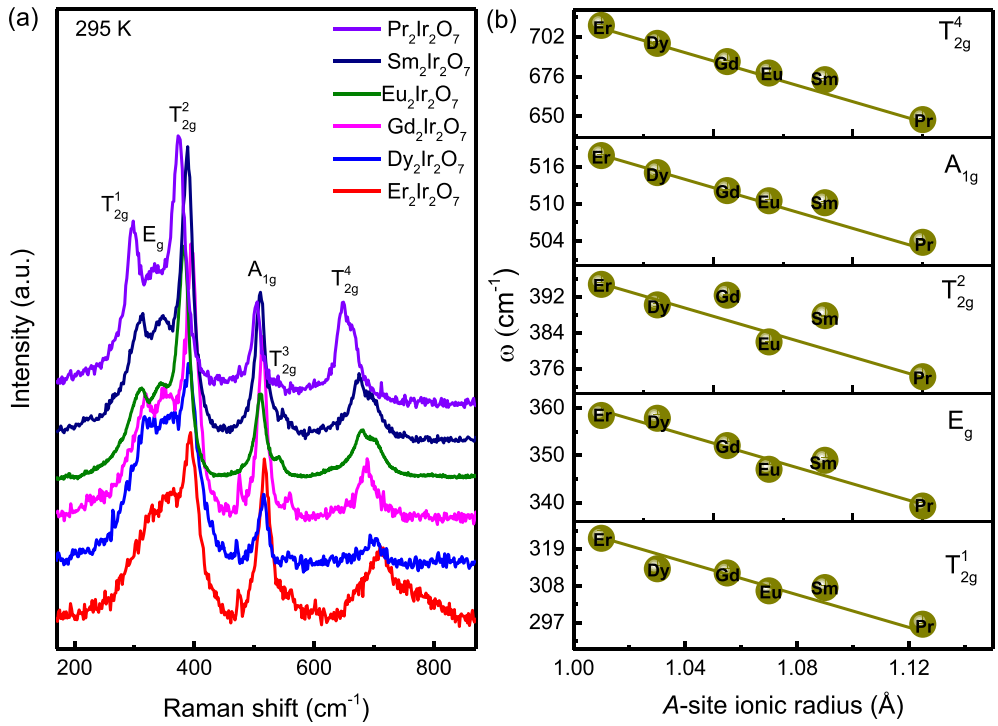

FIG. 2. (a) Ambient Raman spectra of $A_2Ir_2O_7$, (A = Pr [25], Sm, [27] Eu [26], Gd, Dy, and Er) and (b) evolution of the Phonon frequencies with the ionic radius of A-site cation at 295 K (inside the crysostat).

cumulative Lorentz fitting in the range of 50 to 1000 cm^{-1} for all three samples (see Fig. 3). From Figs. 3 and S4, it is clear that there is no change in the number of phonon modes with decreasing temperature as expected for the absence of a structural transition, consistent with temperature-dependent XRD studies [26,51]. However, we have observed two additional modes, N_1 and N_2, below T_N, that become more intense as temperature is lowered. It is noteworthy that N_2 is a broad mode that can be deconvoluted by fitting with an additional mode, as illustrated in Fig. 3, while N_1 is a well-resolved mode in all the three samples. Since the cubic symmetry is preserved at low temperatures, these peaks are unlikely to arise

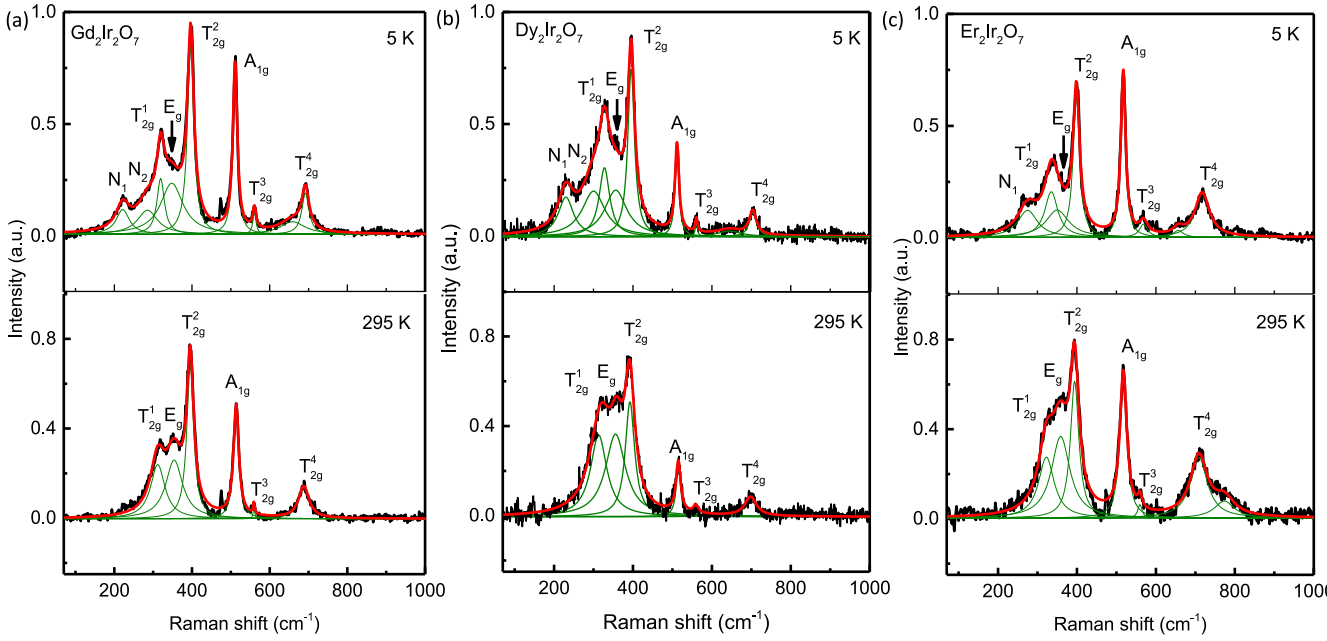

FIG. 3. [(a)–(c)] Fitted Raman spectra of $A_2Ir_2O_7$ (A = Gd, Dy, and Er, respectively) at 5 K (top) and 295 K (bottom). Solid green curves are the individual fit to the phonon modes, and solid red lines are cumulative Lorentz fit to the spectra.

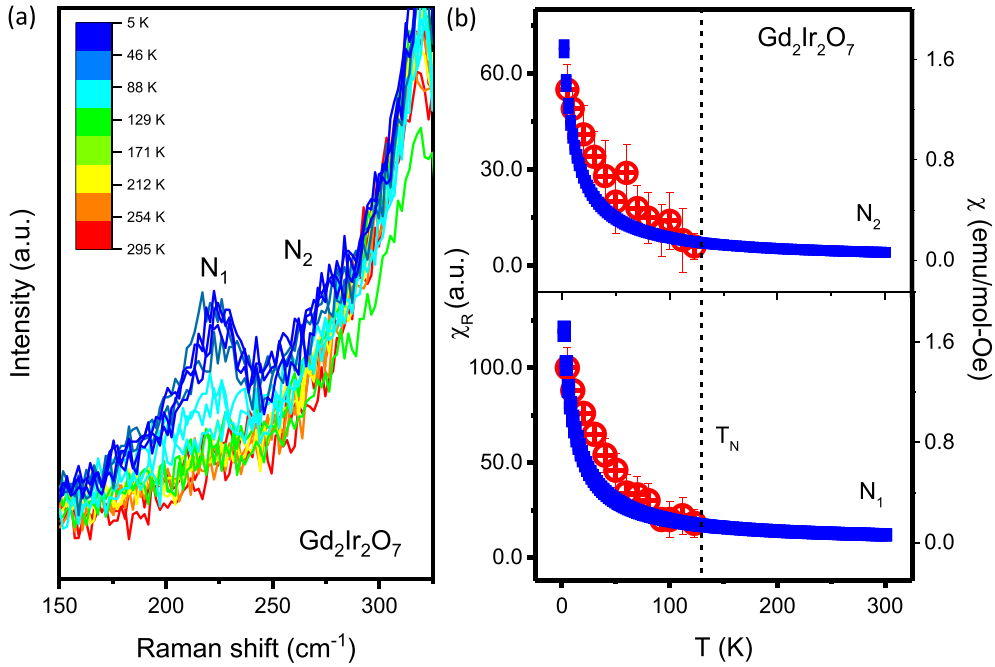

FIG. 4. (a) Temperature evolution of magnon excitations, N_1 and N_2 in $Gd_2Ir_2O_7$, (b) Raman susceptibility of N_1 and N_2 in bottom and top panels, respectively superimposed on the measured magnetic susceptibility for $Gd_2Ir_2O_7$ adopted from Ref. [30], indicated by solid blue curves, vertical black dashed line indicates T_N.

from any lattice distortions. Further, the excitation wavelength dependence of the peaks, as shown in Fig. S5 [14], confirms that the bands N_1 and N_2 are not due to photoluminescence. Since these modes appear only below T_N, they are associated with the magnetic excitations in the AFM-ordered state, as suggested in recent studies [47,52].

D. Single magnon excitation

The presence of N_1 is distinctly evident in Fig. 3, appearing well-resolved, while N_2 appears as a broad mode in both $Gd_2Ir_2O_7$ and $Dy_2Ir_2O_7$. To validate the existence of N_2, we fitted the spectra with and without its inclusion, as illustrated in Figs. S6(a)– S6(d) [14]. It is evident from Fig. S6 [14] that fitting the spectra with two magnon modes (N_1 and N_2) enhances the overall fitting while minimizing the χ^2 values, otherwise known as scale error with square and is equal to the residual sum of square (RSS) divided by the degree of freedom. It can be seen from Fig. S6 [14] that omitting N_2 is causing a notable difference in the fitted and observed curves. Hence, the peak positions are estimated by fitting the spectra while minimizing the difference between the observed data and the fitted curve. Figure 4(a) shows the temperature evolution of N_1 and N_2 for $Gd_2Ir_2O_7$, which shows that as the temperature rises, the peaks are suppressed and become indistinguishable above T_N. The strong temperature dependence and the disappearance of these modes above the AFM ordering temperature indicate the origin of these bands to be magnetic. The suppression of these peaks with elevated temperature is anticipated as the magnetic ordering is destroyed with increasing temperature. To further understand the evolution of these modes, we evaluate the Raman susceptibility by integrating the Raman conductivity ($\chi''(\omega)/\omega$) within a defined frequency range for the individual modes,

$$\chi_R = \lim_{\omega\to 0} \chi(k=0,\omega) \equiv \frac{2}{\pi}\int \frac{\chi''(\omega)}{\omega} d\omega, \qquad (1)$$

where $\chi''(\omega) = I(\omega)/(1+n(\omega))$, $I(\omega)$ is the measured Raman intensity, and $1+n(\omega) = 1/(1-e^{-\hbar\omega/k^{\top}})$ is the Bose thermal factor. Figure 4(b) shows the temperature evolution of the Raman susceptibility of N_1 and N_2 modes, which superimposes very well with the measured magnetic susceptibility curve (Chap. 6 of Ref. [30]), further confirming the magnetic origin of these excitations. Similar peaks have been previously observed for $Eu_2Ir_2O_7$ and $Y_2Ir_2O_7$ close to the magnon dispersion gap energies (within 25 to 35 meV) and have been attributed to single magnon excitation due to the AIAO magnetic ordering at low temperatures [52,53]. We, therefore, assign N_1 and N_2 (at 27.3 and 35.3 meV, respectively) as single magnon excitation in the AFM-ordered state of $Gd_2Ir_2O_7$. The conventional single magnon Raman scattering is caused by the magnetic dipole transition and is difficult to detect because of low scattering efficiency [54]. However, in pseudospin configuration ($J_{\text{eff}} = 1/2$), the electric field can couple to the magnon operators via $H_{ED} = e\sum(d\,E)$ (where e, d, and E denote the electronic charge, ionic displacement from the equilibrium position, and radiation electric field, respectively) and result in a significant scattering amplitude within the second-order time-dependent perturbation theory [52,54,55]. In comparison, the Raman scattering intensity from the electric-dipole transition is about nine times larger than that of the magnetic-dipole transition [55]. The electric dipole transition results in a modification of the unquenched orbital angular momentum within the pseudospin state by ± 1. This change in the orbital angular momentum causes a reversal in the pseudospin direction, resulting in the

occurrence of one magnon scattering [52]. Hence, the detection of single magnon excitations in $A_2Ir_2O_7$ can be attributed to the $J_{\text{eff}} = 1/2$ pseudospin configuration of the Ir spins. The temperature evolution and Raman susceptibilty of these magnon excitations for $Dy_2Ir_2O_7$ and $Er_2Ir_2O_7$ are given in Fig. S7 [14]. The intensity of N_2 mode in $Er_2Ir_2O_7$ could not be extracted as it is not well resolved, as shown in Fig. 3.

We now discuss the estimation of single magnon excitation energies. Typically, the spin Hamiltonian can be written as a sum of the isotropic exchange (IE), Dzyaloshinskii-Moriya (DM), and anisotropic exchange (AE) interactions and has the general form [49,52,56]

$$H_{spin} = \sum_{ij}^{nn} [J_{ij}(S_i \cdot S_j) + D_{ij}(S_i \times S_j) + S_i \cdot A_{ij} \cdot S_j], \quad (2)$$

where J_{ij}, D_{ij}, and A_{ij} are the coefficients of the IE, DM, and AE interactions, respectively, between ith and jth pseudospins of Ir ion denoted by S_i and S_j (nn refers to the nearest neighbor interaction). Since A_{ij} is negligible in the case of pyrochlore iridates [57], the spin Hamiltonian is mainly governed by the first two leading terms. The DM interaction term originates from the SOC and is much larger for 5*d*-iridates as compared to 3*d* and 4*d* transition metal compounds [56,58,59]. Further, the noncolinear spin configurations result in a large $S_i \times S_j$ value in the spin Hamiltonian. It has been previously reported that the magnetic dispersion in $A_2Ir_2O_7$ is fourfold-degenerate and exhibits a gap at the Γ point due to strong DM interaction [28]. The fourfold magnon bands have single and triple degeneracies and the energy levels at the Γ point of the Brillouin zone are given by [28,52]

$$E_1(\Gamma) = 2S\sqrt{\frac{8\sqrt{2}JD + 14D^2}{3}}, \quad (3)$$

$$E_2(\Gamma) = 2S\,3\sqrt{2}D, \quad (4)$$

where E_1 and E_2 refer to triplet and singlet states, respectively. When $E_1 < E_2$, the magnon bands cross at a *k* point along the ΓX lines (protected by $\overline{T_d}$ symmetry) and is called crossing magnon band phase, and when the magnon bands cannot cross in the reverse situation, it is called noncrossing magnon bands. The D/J ratio plays a key role in deciding the magnon band topology as crossing ($D/J > 0.28$) or noncrossing ($D/J < 0.28$) [28]. The observed single magnon excitations N_1 and N_2 in this study can be used to estimate J and D values for $Gd_2Ir_2O_7$ and $Dy_2Ir_2O_7$ (since N_2 is not well resolved in $Er_2Ir_2O_7$) by solving the above two equations. Here, we assign N_1 and N_2 as E_1 and E_2, respectively, similar to the magnon mode assignments in the neighboring pyrochlore $Eu_2Ir_2O_7$ and $Sm_2Ir_2O_7$ (noncrossing magnon bands, i.e., $E_1 > E_2$) [47,52]. The (E_1, E_2) values obtained from the fitting of N_1 and N_2 are (35.3, 24.3) meV and (37.2, 28.5) meV for $Gd_2Ir_2O_7$ and $Dy_2Ir_2O_7$, respectively. The measured values of D and J in this study are close to the measured value of $Tb_2Ir_2O_7$ using RIXS, where J is estimated to be ∼40 meV and $D \sim 3$ meV [60]. This is expected as $Tb_2Ir_2O_7$ lies between $Gd_2Ir_2O_7$ and $Dy_2Ir_2O_7$ in the phase diagram. The estimated J and D values are given in Table I, and the D/J ratio is close to the previously reported values for other pyrochlore iridates from inelastic x-ray scattering (RIXS) experiments and quantum chemistry calculations (QCC) [7,53,56].

TABLE I. Calculated D and J values for $Gd_2Ir_2O_7$ and $Dy_2Ir_2O_7$.

Sample	D	J	D/J
$Gd_2Ir_2O_7$	6.42 ± 0.5	43.53 ± 2.6	0.15 ± 0.014
$Dy_2Ir_2O_7$	6.72 ± 0.6	46.25 ± 2.8	0.14 ± 0.016

Moreover, as illustrated in Fig. S6 [14], magnon modes appear weak and broad compared to phonon modes, posing challenges in precisely estimating energy within the error bars of the measurement and the fitting procedure (as given in Table I). The difference in J values between the two samples is 2.72 meV which lies within the error bars of the experimental data. Hence, instead of exact values, we infer that the approximate D/J ratio falls within the expected range derived from magnon dispersion. Given the similarity in ionic radii and transition temperature between Gd and Dy iridates, we expect minimal changes in their structural and magnetic properties, reflected in the nearly same D/J. Further theoretical calculations and experiments capable of directly probing magnetic order and estimating exact interaction values are required in future studies.

E. Temperature-dependent phonon anomalies

We now discuss the temperature dependence of phonon frequencies and line widths shown in Figs. 5–7. To quantify the temperature dependence of the phonon modes, we use a simple cubic anharmonic model of phonon self-energies, which involves the decay of an optical phonon into two phonons of equal frequencies ($\omega_0/2$) and is given by [61]

$$\omega(T) = \omega_0 + C[1 + 2n(\omega_0/2)], \quad (5)$$

$$\Gamma(T) = \Gamma_0 + D[1 + 2n(\omega_0/2)], \quad (6)$$

where n ($\omega_0/2$) is the Bose factor, and the parameters C (−ve) and D (+ve) are related to the phonon-phonon interaction strength. The solid red lines in Figs. 5–7 fit to the cubic anharmonic model above T_N, extrapolated by dotted lines to low temperatures. The observed phonon frequencies and linewidth, exhibit significant deviations from the anharmonic model calculations, as can be seen, signifying additional contributions to the phonon self-energy. In general, the total phonon self-energy has three contributions: phonon-phonon, electron-phonon, and spin-phonon interactions. The real (imaginary) part of self-energy gives changes in phonon frequency (linewidth) with temperature. The phonon-phonon part is a monotonic function of temperature and cannot result in phonon anomalies below T_N. Since the samples are insulating in the antiferromagnetic state, the electron-phonon contribution will also be negligible. This is also evident from the absence of any electronic Raman scattering or Fano resonance at low temperatures. This implies that the spin-phonon coupling is the dominant mechanism in understanding the anomalies below T_N. To gain a better understanding, we will now go over temperature-dependent phonon behavior in detail for each sample.

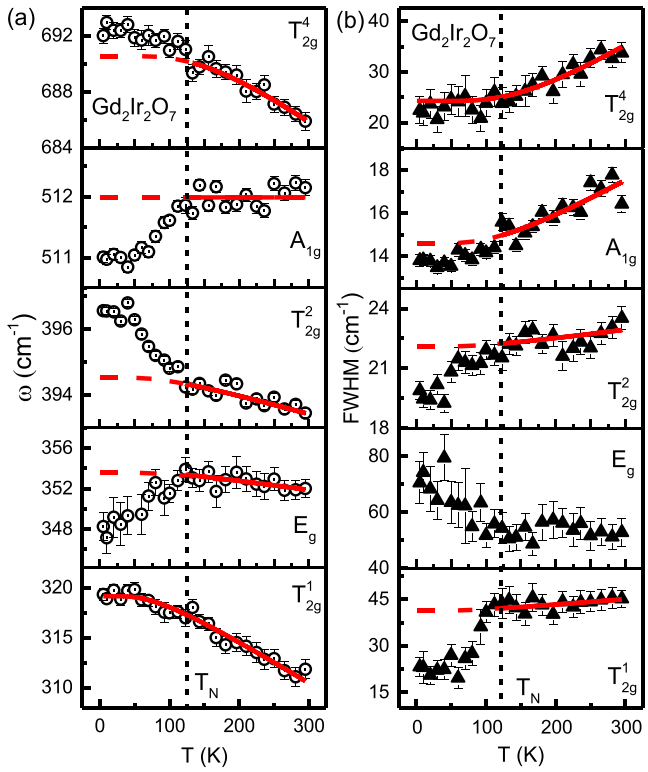

FIG. 5. [(a) and (b)] Temperature dependence of phonon frequencies and linewidths for $Gd_2Ir_2O_7$, respectively. Solid red lines are fit to the anharmonic model above T_N and red dashed lines are the fitting extrapolated to zero Kelvin. The vertical black dashed line indicates T_N.

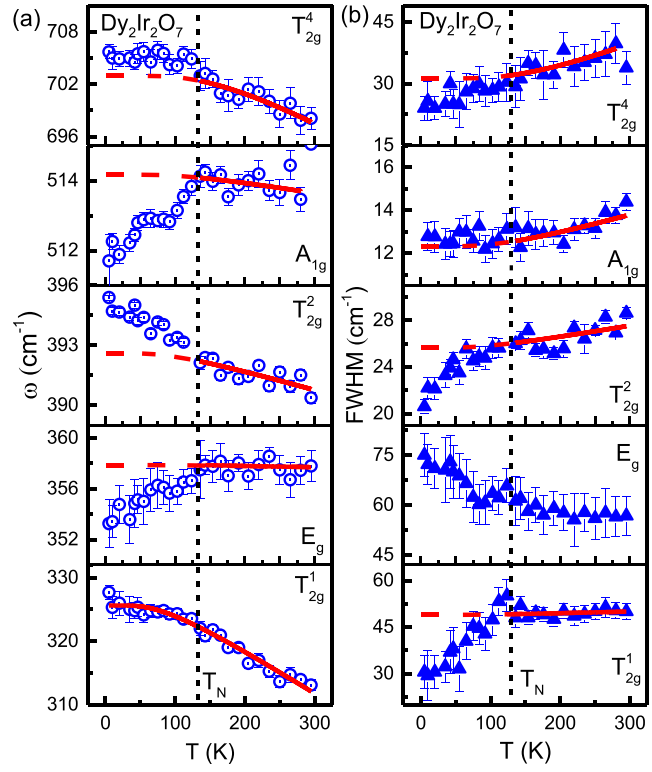

FIG. 6. [(a) and (b)] Temperature dependence of phonon frequencies and linewidths for $Dy_2Ir_2O_7$, respectively. Symbols have the same meaning as Fig. 5.

(i) *Phonon anomalies for* $Gd_2Ir_2O_7$. It can be seen from Fig. 5 that all phonons show anomalous behavior below T_N (123 K). The most noticeable observation is an Ir-O-Ir vibration E_g phonon, which shows anomalous softening of ∼5 cm^{-1} below T_N, and its linewidth shows anomalous broadening by a significant amount (∼18 cm^{-1}) with decreasing temperature. Further, the Ir-O-Ir vibration A_{1g} phonon also shows similar frequency softening (∼1 cm^{-1}) below T_N. Additional noteworthy observations below T_N are (i) deviation of T^2_{2g} (∼2 cm^{-1}) and T^4_{2g} (∼2 cm^{-1}) modes from the anharmonic fit and (ii) the linewidth of T^1_{2g} mode showing a large decrease (∼20 cm^{-1}) below T_N than predicted by the anharmonic model. Further, the linewidth drop in the T^1_{2g} phonon is similar to our previous studies on $Eu_2Ir_2O_7$ [26].

(ii) *Phonon anomalies for* $Dy_2Ir_2O_7$. For $Dy_2Ir_2O_7$ (T_N = 130 K), all the modes deviate from the anharmonic model below T_N as shown in Fig. 6, similar to $Gd_2Ir_2O_7$. Overall, the spin-phonon coupling is similar in $Gd_2Ir_2O_7$ and $Dy_2Ir_2O_7$.

(iii) *Phonon anomalies for* $Er_2Ir_2O_7$. For $Er_2Ir_2O_7$ (T_N = 137 K), Figs. 7(a) and 7(b) show the temperature dependence of phonon frequencies and linewidths. The overall trends in the anomalous behavior are similar to Gd and Dy iridates. In addition, the linewidth of T^4_{2g} phonon shows significant deviation below T_N, not observed in the case of $Gd_2Ir_2O_7$ and $Dy_2Ir_2O_7$. Given the weak shoulder modes of the T^4_{2g}, we can not rule out that the linewidth may be influenced by the second-order modes in the fitting process of this peak.

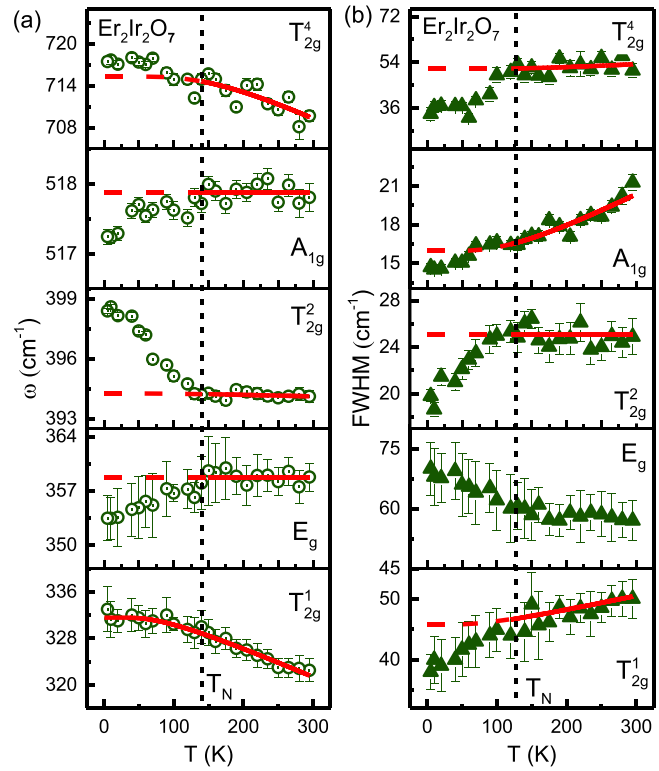

FIG. 7. [(a) and (b)] Temperature dependence of phonon frequencies and linewidths for $Er_2Ir_2O_7$, respectively. Symbols have the same meaning as Fig. 5.

Unlike 3*d* and 4*d* transition metal oxides [62–64], $A_2Ir_2O_7$ (A = Gd, Dy, and Er) show large frequency shifts and exceptionally high linewidth variation in all of the phonon modes. Similar large phonon renormalizations below T_N have been reported in a number of pyrochlores and have been attributed to efficient magnetoelastic coupling due to the strong spin-orbit coupling-driven contribution to magnetism [65]. It is clear from the above data that the Ir-O-Ir bending modes (A_{1g} and E_g) are getting most affected by the spin-phonon coupling similar to previous reports of E_g mode in of $Eu_2Ir_2O_7$ [47], A_{1g} and E_g in the Raman study of $(Sm_{1-x}Bi_x)_2Ir_2O_7$ [27], A_{1g} mode in $(Eu_{1-x}Bi_x)_2Ir_2O_7$ [26], Ir-O stretching mode in $Cd_2Os_2O_7$ [65], the A_{1g} and Ir-O stretching modes in $Y_2(Ir_{1-x}Ru_x)_2O_7$ [66], and three Ir-O-Ir infrared phonons in $Y_2Ir_2O_7$ [49]. These renormalizations are primarily arising from strong spin-phonon coupling in the spin-ordered state due to the phonon modulation of the spin-exchange interactions (J_{ij} and D_{ij}). The modulation of J_{ij} by the vibrational amplitude (r) and bond angle (θ) of Ir-O interactions influences the exchange interaction, leading to the renormalization of a specific phonon frequency. The corresponding value is denoted as $\Delta\omega \sim \lambda_{IE}(S_i \cdot S_j)$, where λ_{IE} is proportionate to $\frac{\partial^2 J_{ij}(\theta)}{\partial\theta^2}$ and $\frac{\partial^2 J_{ij}(r)}{\partial r^2}$ [49,67]. The sign of λ_{IE} can be negative or positive depending on the phonon modes. However, the spin-phonon coupling due to the DM interaction arises from the modulation of D_{ij} with respect to the Ir-O-Ir bond angle (θ). The phonon renormalization $\Delta\omega$ is proportional to $\sum_{ij} \frac{\partial^2 D_{ij}(\theta)}{\partial\theta^2} \cdot (S_i \times S_j)$. The sign of D represents the chirality of spin texture. A spin-phonon contribution is caused by modulation of spin exchange energy by zone-center lattice vibrations below magnetic ordering temperature and is given as [49,68,69],

$$\Delta\omega_{SPC} \sim \frac{-2}{I_R\omega}\left[\sum_{ij}^{nn} \frac{\partial^2 J_{ij}(\theta, r)}{\partial v^2} \cdot < S_i \cdot S_j > + \sum_{ij}^{nn} \frac{\partial^2 D_{ij}(\theta, r)}{\partial v^2} \cdot < S_i \times S_j >\right], \quad (7)$$

where I_R is the rotational moment of inertia and v the bond angle (θ) or bond length (r) following the type of vibration. The softening or hardening of phonons is determined by the sign of $\Delta\omega_{SPC}$. The strength of the spin-phonon coupling will vary depending on the modulation of the exchange energy concerning the atomic displacement. Hence, phonon renormalization will be different for different phonon modes. In this context, the renormalization of the Ir-O stretching mode can be related to the modulation of the IE interaction as in conventional spin-phonon coupling in 3*d* multiferroic manganates, $RMnO_3$ (R = Pr, Nd, Sm, Eu, Gd, Tb, Dy, Ho, and Y) [64], 4*d*-pyrochlore Y_2Ru_2O [63], and some 3*d*-chromates, $CdCr_2O_4$ and $ZnCr_2O_4$ [62]. Similarly, the phonon renormalization for the bending modes is related to the modulation of the DM interaction, as in $Y_2Ir_2O_7$ and $Eu_2Ir_2O_7$ [47,49]. The orbital overlap integral can be significantly modified by a change in the bond length of Ir-O which, in turn, can alter the spin exchange energy and cause phonon frequency renormalization [22,68]. Hence, the hardening of the stretching modes, T_{2g}^2 and the T_{2g}^4 is attributed to the positive sign of λ_{IE}. Further, considering the softening of E_g and A_{1g} phonons, a previous study by Son *et al*. showed that the Ir-O-Ir bending motion is strongly correlated with θ-dependent J and D modulations as they involve the motion of all oxygen ions between the nearest-neighboring Ir ions within the Ir-O-Ir plane and perpendicular to the Ir-Ir bond. Thus the modulation of θ due to atomic vibration can result in large softenings by modulating both J and D. However, it has been shown that in pyrochlore iridates, the DM interaction contributes an order of magnitude larger than the IE interaction [49]. Hence, the softening of the bending modes, (A_{1g} and E_g) mostly arises due to the negative sign of $\frac{\partial^2 D_{ij}(\theta)}{\partial\theta^2}$ below T_N.

Figure 8 shows spin-phonon contribution driven by DM interaction extracted by subtracting the observed value from the calculated value based on the anharmonic interaction, $\Delta\omega_{SPC} = \omega_{anharmonic} - \omega_{experimental}$ for the bending vibration modes below T_N. This demonstrates that the DM interaction plays a significant role in causing large phonon shifts below T_N. This is understandable, given that the DM interaction term is derived from the SOC [58]. The SOC is a relativistic interaction that changes as z^2, where z is the atomic number [59]. As a result, the SOC energy is greater for heavy elements. The SOC energy of 5*d* transition metal oxides is ~500 meV, significantly greater than the SOC energy of 3*d* transition metal oxides (<10 meV) [49]. As a result, the strong SOC-induced DM interaction in the noncolinear AIAO magnetic ordered state can result in such unconventional spin-phonon coupling in pyrochlore iridates.

F. Phonon and magnon excitations in $A_2Ir_2O_7$

In the AIAO-ordered state, the collective behavior of spins allows for the propagation of spin waves, namely magnons, through the magnetic lattice. These magnons can be probed experimentally using techniques such as inelastic neutron scattering or Raman spectroscopy, where they appear in the spectrum corresponding to the energy and momentum of the magnon excitations. Pyrochlore iridates $A_2Ir_2O_7$ present a unique system wherein magnetic interactions can be finely tuned by manipulating small structural details with the A-site cation to create a desired topological phase. Moreover, the magnon excitations in iridates are Raman active due to the strong spin-orbit coupling and consequent noncoplanar magnetic ordering pattern.

Numerous studies have documented magnon dispersion in iridates. For instance, Ueda *et al.* conducted a Raman study on $Eu_2Ir_2O_7$ [47], reporting single magnon excitations in the AIAO state. Additionally, our previous research on $Eu_2Ir_2O_7$ [26], and that of Nguyen *et al.* [52], observed magnon excitations in various iridates, including $Y_2Ir_2O_7$, $Eu_2Ir_2O_7$, and $Sm_2Ir_2O_7$. In our previous study on $Sm_2Ir_2O_7$, the detection of magnon peaks was hindered by a broad underlying continuum attributed to spin-spin correlations within the AIAO state [27]. Notably, $Pr_2Ir_2O_7$ lacks magnetic ordering; thus, magnon excitations are not observed in this compound [25,70]. In conventional single magnon Raman scattering, detection is challenging due to the low scattering efficiency arising from magnetic dipole transitions. However, in the pseudospin configuration in $A_2Ir_2O_7$, Raman scattering

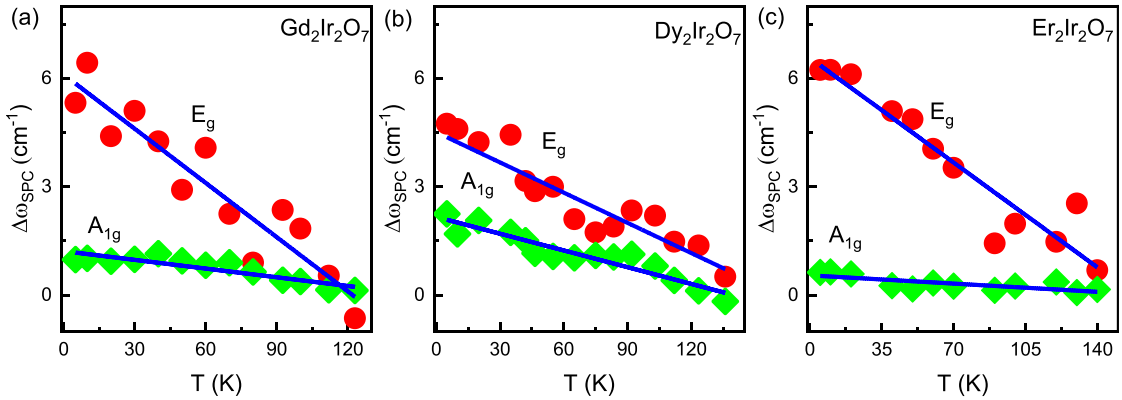

FIG. 8. [(a)–(c)] The $\Delta\omega_{SPC} = \omega_{anharmonic} - \omega_{experimental}$ for Ir-O-Ir bending modes below T_N for $Gd_2Ir_2O_7$, $Dy_2Ir_2O_7$, and $Er_2Ir_2O_7$, respectively, solid blue lines are guide to the eye.

intensity arises from electric-dipole transitions, significantly enhancing detection sensitivity. Hence, single magnon excitations in $A_2Ir_2O_7$ can be observed in Raman scattering. However, the occurrence of magnon excitations in different iridates may be dependent upon various additional factors, including the strength of magnetic interactions, the presence of magnetic impurities or defects, and environmental conditions such as temperature and pressure. Additionally, the signal-to-noise ratio can impact the detectability of these excitations as magnon bands are usually weaker as compared to phonons. Further, the visibility of magnon modes may vary across different polarization configurations in single crystals, depending upon Raman selection rules.

The physical characteristics of $A_2Ir_2O_7$ compounds evolve with the A-site cation radius, transitioning from magnetic insulating behavior $Ho_2Ir_2O_7$ to $Nd_2Ir_2O_7$ to a complex nonmagnetic metallic state in $Pr_2Ir_2O_7$. Since the rare earth spins in case of magnetic A-sublattice order at a much lower temperature (10–15 K), the temperature range of our focus, primarily addressing the ordering temperature range (100–150 K), stands considerably distinct from the A-site ordering temperature, with only Ir magnetic moments contributing significantly to the observed phonon dynamics. The phonon self-energies are influenced by electron-phonon and spin-phonon interactions alongside phonon-phonon interactions. Consequently, the phonon dynamics varies significantly for each material in the $A_2Ir_2O_7$ series, contingent upon the underlying physics driving the anomalies. For instance, in our previous study on $Pr_2Ir_2O_7$ [25], electron-phonon coupling dominated, given its transition into a quadratic band touching Luttinger semimetal at low temperatures. Conversely, in the cases of pristine and up to 3.5% (2%) Bi-doped $Eu_2Ir_2O_7$ ($Sm_2Ir_2O_7$) [26,27], the physics differed due to their respective MIT and topological crossover to a Weyl semimetal state, resulting in two distinct temperature scales, T_N and T^* ($T^* < T_N$). Below T_N, spin-phonon coupling predominated, while for $T < T^* < T_N$, the interplay of spin-phonon and electron-phonon interactions, in addition to phonon-phonon interaction, led to behavior very different from conventional spin-phonon or electron-phonon interactions. However, with further Bi doping, the system transitioned into a quadratic band touching state similar to $Pr_2Ir_2O_7$, influenced by strong electron-phonon interaction.

The materials investigated in this manuscript (Gd, Dy, and Er iridates) are situated close to each other in the phase diagram (Fig. S1) [14], exhibiting similar physical properties. Further, the frequencies of the phonon modes also lie in close proximity for these iridates, as shown in Fig. 2(b). Due to the AIAO ordering at low temperatures, the phonons in this study are renormalized by spin-phonon coupling and phonon-phonon interaction below and above T_N, respectively. As all these materials exhibit a metallic nature at room temperature, transitioning into an insulating phase at low temperature, the electron-phonon coupling is absent below T_N. Therefore, owing to similar interactions, the phonon behavior is similar across these materials, with a shift in the temperature range where phonon anomalies are observed, as shown in Figs. 5–7. Furthermore, when considering the iridates examined in this study alongside the nonmagnetic A-site iridates, such as $Eu_2Ir_2O_7$ it is expected that the phonons unaffected by electron-phonon coupling in the WSM state of $Eu_2Ir_2O_7$ (T_{2g}^1 and T_{2g}^2) [47] will demonstrate significant similarity to that of Gd-Er iridates. This similarity arises from the effect of spin-phonon coupling on phonon renormalization. The analogous behavior observed in the T_{2g} phonons between nonmagnetic Eu and magnetic iridates supports the conclusion that only the magnetic moments of Ir contribute to the observed phonon dynamics. These distinctions and similarities underscore the nontrivial phonon behavior of iridate compounds.

IV. CONCLUSIONS

In summary, the emergence of single magnon excitations within the AIAO-ordered state corroborates the magnetic behavior of these iridates. Through the analysis of magnon energies, we have estimated the IE and DM interaction parameter (J and D, respectively), revealing D/J to be ∼0.15 for $Gd_2Ir_2O_7$ and $Dy_2Ir_2O_7$. The anomalous frequency softening observed in the Ir-O-Ir bond bending vibrations (A_{1g} and E_g) below T_N is attributed to the spin-phonon interaction induced by the phonon modulation of the DM spin-exchange interaction. Additionally, significant hardening of the stretching modes T_{2g}^2 and T_{2g}^4 in the magnetic insulating phase further underscores the intricate interplay of spin and lattice dynamics

in these materials. These observations collectively establish the presence of magnon excitations and strong spin-phonon coupling in the AIAO-ordered state for the studied pyrochlore iridates. Our experimental findings contribute to the understanding of the complex interplay between magnetic and vibrational properties in pyrochlore iridates, paving the way for further investigations and potential applications in the area of spintronics and magnonics.

ACKNOWLEDGMENTS

A.K.S. thanks the Department of Science and Technology, Government of India, for financial support under the National Science Chair Professorship. M.R. would like to thank the Micro Nano Characterization facility (MNCF) at the Center for Nanoscience and Engineering (CeNSE) IISc and the Indian Science Technology and Engineering Facilities Map (I-STEM) for material characterization.

[1] X. Wan, A. M. Turner, A. Vishwanath, and S. Y. Savrasov, Topological semimetal and Fermi-arc surface states in the electronic structure of pyrochlore iridates, Phys. Rev. B **83**, 205101 (2011).

[2] W. Witczak-Krempa and Y. B. Kim, Topological and magnetic phases of interacting electrons in the pyrochlore iridates, Phys. Rev. B **85**, 045124 (2012).

[3] K. Ueda, T. Oh, B.-J. Yang, R. Kaneko, J. Fujioka, N. Nagaosa, and Y. Tokura, Magnetic-field induced multiple topological phases in pyrochlore iridates with Mott criticality, Nat. Commun. **8**, 15515 (2017).

[4] L. Savary, E.-G. Moon, and L. Balents, New type of quantum criticality in the pyrochlore iridates, Phys. Rev. X **4**, 041027 (2014).

[5] B. Ma, B. Flebus, and G. A. Fiete, Longitudinal spin Seebeck effect in pyrochlore iridates with bulk and interfacial Dzyaloshinskii-Moriya interaction, Phys. Rev. B **101**, 035104 (2020).

[6] J. P. Clancy, H. Gretarsson, E. K. H. Lee, D. Tian, J. Kim, M. H. Upton, D. Casa, T. Gog, Z. Islam, B.-G. Jeon, K. H. Kim, S. Desgreniers, Y. B. Kim, S. J. Julian, and Y.-J. Kim, X-ray scattering study of pyrochlore iridates: Crystal structure, electronic, and magnetic excitations, Phys. Rev. B **94**, 024408 (2016).

[7] C. Donnerer, M. C. Rahn, M. M. Sala, J. G. Vale, D. Pincini, J. Strempfer, M. Krisch, D. Prabhakaran, A. T. Boothroyd, and D. F. McMorrow, All-in–all-out magnetic order and propagating spin waves in $Sm_2Ir_2O_7$, Phys. Rev. Lett. **117**, 037201 (2016).

[8] Y. Wang, T. F. Rosenbaum, D. Prabhakaran, A. T. Boothroyd, and Y. Feng, Approaching the quantum critical point in a highly correlated all-in–all-out antiferromagnet, Phys. Rev. B **101**, 220404(R) (2020).

[9] S. Nakatsuji, Y. Machida, Y. Maeno, T. Tayama, T. Sakakibara, J. van Duijn, L. Balicas, J. N. Millican, R. T. Macaluso, and J. Y. Chan, Metallic spin-liquid behavior of the geometrically frustrated kondo lattice $Pr_2Ir_2O_7$, Phys. Rev. Lett. **96**, 087204 (2006).

[10] H. Zhang, K. Haule, and D. Vanderbilt, Metal-insulator transition and topological properties of pyrochlore iridates, Phys. Rev. Lett. **118**, 026404 (2017).

[11] K. Matsuhira, M. Wakeshima, R. Nakanishi, T. Yamada, A. Nakamura, W. Kawano, S. Takagi, and Y. Hinatsu, Metal–insulator transition in pyrochlore iridates $Ln_2Ir_2O_7$ (Ln = Nd, Sm, and Eu), J. Phys. Soc. Jpn. **76**, 043706 (2007).

[12] K. Matsuhira, M. Wakeshima, Y. Hinatsu, and S. Takagi, Metal–insulator transitions in pyrochlore oxides $Ln_2Ir_2O_7$, J. Phys. Soc. Jpn. **80**, 094701 (2011).

[13] M. Graf, S. Disseler, C. Dhital, T. Hogan, M. Bojko, A. Amato, H. Luetkens, C. Baines, D. Margineda, S. Giblin, M. Jura, and S. Wilson, Magnetism and magnetic order in the pyrochlore iridates in the insulator-to-metal crossover region, J. Phys.: Conf. Ser. **551**, 012020 (2014).

[14] See Supplemental Material at http://link.aps.org/supplemental/10.1103/PhysRevB.109.184434 for information on the phase diagram (Fig. S1), Rietveld refined parameters (Fig. S2), XPS data (Fig. S3), and supporting figures for temperature-dependent Raman studies (Figs. S4–S7).

[15] R. Asih, N. Adam, S. S. Mohd-Tajudin, D. P. Sari, K. Matsuhira, H. Guo, M. Wakeshima, Y. Hinatsu, T. Nakano, Y. Nozue, S. Sulaiman, M. I. Mohamed-Ibrahim, P. K. Biswas, and I. Watanabe, Magnetic moments and ordered states in pyrochlore iridates $Nd_2Ir_2O_7$ and $Sm_2Ir_2O_7$ Studied by Muon-Spin Relaxation, J. Phys. Soc. Jpn. **86**, 024705 (2017).

[16] H. Han, L. Zhang, H. Liu, L. Ling, W. Tong, Y. Zou, M. Ge, J. Fan, C. Zhang, L. Pi, and Y. Zhang, Electron paramagnetic resonance study of the $f - d$ interaction in pyrochlore iridate $Gd_2Ir_2O_7$, Philos. Mag. **95**, 3014 (2015).

[17] D. Staško, K. Vlášková, P. Proschek, and M. Klicpera, Conductive properties of heavy-rare-earth $A_2Ir_2O_7$ iridates synthesized by the CsCl-flux method, J. Phys. Chem. Solids **176**, 111268 (2023).

[18] M. Klicpera, K. Vlášková, and M. Diviš, Characterization and magnetic properties of heavy rare-earth $A_2Ir_2O_7$ pyrochlore iridates, the case of $Tm_2Ir_2O_7$, J. Phys. Chem. C **124**, 20367 (2020).

[19] X. Moya and N. D. Mathur, Turn your phonon, Nat. Mater. **16**, 784 (2017).

[20] R. Ramesh and N. A. Spaldin, Multiferroics: progress and prospects in thin films, Nat. Mater. **6**, 21 (2007).

[21] W. Eerenstein, N. D. Mathur, and J. F. Scott, Multiferroic and magnetoelectric materials, Nature (London) **442**, 759 (2006).

[22] X. Wan, H.-C. Ding, S. Y. Savrasov, and C.-G. Duan, Short range magnetic exchange interaction favors ferroelectricity, Sci. Rep. **6**, 22743 (2016).

[23] J. H. Lee, L. Fang, E. Vlahos, X. Ke, Y. W. Jung, L. F. Kourkoutis, J.-W. Kim, P. J. Ryan, T. Heeg, M. Roeckerath, V. Goian, M. Bernhagen, R. Uecker, P. C. Hammel, K. M. Rabe, S. Kamba, J. Schubert, J. W. Freeland, D. A. Muller, C. J. Fennie *et al.*, A strong ferroelectric ferromagnet created by means of spin–lattice coupling, Nature (London) **466**, 954 (2010).

[24] M. Mochizuki, N. Furukawa, and N. Nagaosa, Theory of spin-phonon coupling in multiferroic manganese perovskites $R\mathrm{MnO}_3$, Phys. Rev. B **84**, 144409 (2011).

[25] M. Rosalin, P. Telang, S. Singh, D. V. S. Muthu, and A. K. Sood, Non-Fermi-liquid signatures of quadratic band touching and phonon anomalies in metallic $Pr_2Ir_2O_7$, Phys. Rev. B **108**, 195144 (2023).

[26] A. Thomas, P. Telang, K. Mishra, M. Cesnek, J. Bednarcik, D. V. S. Muthu, S. Singh, and A. K. Sood, Role of spin-phonon and electron-phonon interactions in the phonon renormalization of $(Eu_{1-x}Bi_x)_2Ir_2O_7$ across the metal-insulator phase transition: Temperature-dependent Raman and x-ray studies, Phys. Rev. B **105**, 075145 (2022).

[27] M. Rosalin, P. Telang, S. Singh, D. V. S. Muthu, and A. K. Sood, Raman signatures of quadratic band touching state and strong spin-phonon coupling in pyrochlore iridates $(Sm_{1-x}Bi_x)_2Ir_2O_7$, Phys. Rev. B **108**, 035133 (2023).

[28] K. Hwang, N. Trivedi, and M. Randeria, Topological magnons with nodal-line and triple-point degeneracies: Implications for thermal hall effect in pyrochlore iridates, Phys. Rev. Lett. **125**, 047203 (2020).

[29] H. S. Rajeev, P. Telang, and S. Singh, One-shot wet chemical synthesis and physical properties of pyrochlore iridates $A_2Ir_2O_7$, (A = Sm, Gd, Dy and Er), Solid State Commun. **312**, 113863 (2020).

[30] P. Telang, Tuning the ground state of pyrochlore oxides using chemical pressure, Ph.D. thesis, Indian Institute of Science Education and Research (IISER) Pune, 2020.

[31] K. Vlášková, M. Diviš, and M. Klicpera, The magnetic behaviour of $Dy_2Ir_2O_7$ - Beyond the mean field approximation, J. Magn. Magn. Mater. **538**, 168220 (2021).

[32] K. Vlášková, P. Proschek, M. Diviš, D. Le, R. H. Colman, and M. Klicpera, Magnetic properties and crystal field splitting of the rare-earth pyrochlore $Er_2Ir_2O_7$, Phys. Rev. B **102**, 054428 (2020).

[33] L. A. Deschenes, Origin 6.0: scientific data analysis and graphing software origin lab corporation (formerly Microcal Software, Inc.). Web site: www.originlab.com., J. Am. Chem. Soc. **122**, 9567 (2000).

[34] P. Telang, K. Mishra, A. K. Sood, and S. Singh, Dilute stuffing in the pyrochlore iridate $Eu_2Ir_2O_7$, Phys. Rev. B **97**, 235118 (2018).

[35] M. Subramanian, G. Aravamudan, and G. S. Rao, Oxide pyrochlores-A review, Prog. Solid State Chem. **15**, 55 (1983).

[36] P. Telang and S. Singh, Protracting the Weyl phase by a giant negative lattice expansion in Bi doped $Sm_2Ir_2O_7$, arXiv:2106.03512.

[37] K. Lee, D. Seo, and M. Whangbo, Structural and electronic factors governing the metallic and nonmetallic properties of the pyrochlores $A_2Ru_2O_{7-y}$, J. Solid State Chem. **131**, 405 (1997).

[38] F. F. Tafti, J. J. Ishikawa, A. McCollam, S. Nakatsuji, and S. R. Julian, Pressure-tuned insulator to metal transition in $Eu_2Ir_2O_7$, Phys. Rev. B **85**, 205104 (2012).

[39] H. Kumar, K. C. Kharkwal, K. Kumar, K. Asokan, A. Banerjee, and A. K. Pramanik, Magnetic and transport properties of the pyrochlore iridates $(Y_{1-x}Pr_x)_2Ir_2O_7$: Role of $f-d$ exchange interaction and $d-p$ orbital hybridization, Phys. Rev. B **101**, 064405 (2020).

[40] A. Kar and S. Elizabeth, Role of R-site magnetic moment in spin-phonon coupling in the pyrochlore iridates $R_2Ir_2O_7$: Magnetic and Raman spectroscopic investigations, Phys. Rev. B **108**, 134426 (2023).

[41] E. Feng, Magnetic order and excitation in frustrated pyrochlore 5*d* - transition metal oxides, Schriften des Forschungszentrums Jülich. Reihe Schlüsseltechnologien / Key Technologies, **187**, IV, 182 S. (2018).

[42] W. Liu, H. Han, L. Ma, L. Pi, L. Zhang, and Y. Zhang, Different pressure effects in $A_2Ir_2O_7$ (A=Gd, Eu, and Sm), J. Alloys Compd. **741**, 182 (2018).

[43] M. Das, S. Bhowal, J. Sannigrahi, A. Bandyopadhyay, A. Banerjee, G. Cibin, D. Khalyavin, N. Banerjee, D. Adroja, I. Dasgupta, and S. Majumdar, Interplay between structural, magnetic, and electronic states in the pyrochlore iridate $Eu_2Ir_2O_7$, Phys. Rev. B **105**, 134421 (2022).

[44] P. Telang, A. Bandyopadhyay, K. Mishra, D. Rout, R. Bag, A. Gloskovskii, Y. Matveyev, and S. Singh, X-ray photoemission and absorption study of the pyrochlore iridates $(Eu_{1-x}Bi_x)_2Ir_2O_7$, $0 \leqslant x \leqslant 1$, J. Phys.: Condens. Matter **34**, 395601 (2022).

[45] H. Kumar, R. S. Dhaka, and A. K. Pramanik, Evolution of structure, magnetism, and electronic transport in the doped pyrochlore iridate $Y_2Ir_{2-x}Ru_xO_7$, Phys. Rev. B **95**, 054415 (2017).

[46] M. S. Khan, I. Carlomagno, C. Meneghini, P. K. Biswas, F. Bert, S. Majumdar, and S. Ray, Mixed-valent metallic pyrochlore iridate: A possible route to non-Fermi liquids, Phys. Rev. B **105**, 085137 (2022).

[47] K. Ueda, R. Kaneko, A. Subedi, M. Minola, B. J. Kim, J. Fujioka, Y. Tokura, and B. Keimer, Phonon anomalies in pyrochlore iridates studied by Raman spectroscopy, Phys. Rev. B **100**, 115157 (2019).

[48] M. L. Sanjuán, C. Guglieri, S. Díaz-Moreno, G. Aquilanti, A. F. Fuentes, L. Olivi, and J. Chaboy, Raman and x-ray absorption spectroscopy study of the phase evolution induced by mechanical milling and thermal treatments in $R_2Ti_2O_7$ pyrochlores, Phys. Rev. B **84**, 104207 (2011).

[49] J. Son, B. C. Park, C. H. Kim, H. Cho, S. Y. Kim, L. J. Sandilands, C. Sohn, J.-G. Park, S. J. Moon, and T. W. Noh, Unconventional spin-phonon coupling via the Dzyaloshinskii-Moriya interaction, npj Quantum Mater. **4**, 17 (2019).

[50] C. L. Tracy, J. Shamblin, S. Park, F. Zhang, C. Trautmann, M. Lang, and R. C. Ewing, Role of composition, bond covalency, and short-range order in the disordering of stannate pyrochlores by swift heavy ion irradiation, Phys. Rev. B **94**, 064102 (2016).

[51] H. Takatsu, K. Watanabe, K. Goto, and H. Kadowaki, Comparative study of low-temperature x-ray diffraction experiments on $R_2Ir_2O_7$ (R = Nd, Eu, and Pr), Phys. Rev. B **90**, 235110 (2014).

[52] T. H. Nguyen, J. Son, S. Kim, H. Cho, C. H. Kim, Y. P. Wang, K. S. Burch, I.-S. Yang, J. Jeong, J.-G. Park, S. J. Moon, and T. W. Noh, Topological magnon band crossing in $Y_2Ir_2O_7$, Phys. Rev. Lett. **127**, 267203 (2021).

[53] S. H. Chun, B. Yuan, D. Casa, J. Kim, C.-Y. Kim, Z. Tian, Y. Qiu, S. Nakatsuji, and Y.-J. Kim, Magnetic excitations across the metal-insulator transition in the pyrochlore iridate $Eu_2Ir_2O_7$, Phys. Rev. Lett. **120**, 177203 (2018).

[54] P. A. Fleury and R. Loudon, Scattering of light by one- and two-magnon excitations, Phys. Rev. **166**, 514 (1968).

[55] R. Elliott and R. Loudon, The possible observation of electronic Raman transitions in crystals, Phys. Lett. **3**, 189 (1963).

[56] R. Yadav, M. Pereiro, N. A. Bogdanov, S. Nishimoto, A. Bergman, O. Eriksson, J. van den Brink, and L. Hozoi, Heavy-mass magnetic modes in pyrochlore iridates due to dominant

Dzyaloshinskii-Moriya interaction, Phys. Rev. Mater. **2**, 074408 (2018).

[57] H. Shinaoka, T. Miyake, and S. Ishibashi, Noncollinear magnetism and spin-orbit coupling in 5*d* pyrochlore oxide $Cd_2Os_2O_7$, Phys. Rev. Lett. **108**, 247204 (2012).

[58] T. Moriya, Anisotropic superexchange interaction and weak ferromagnetism, Phys. Rev. **120**, 91 (1960).

[59] K. V. Shanavas, Z. S. Popović, and S. Satpathy, Theoretical model for Rashba spin-orbit interaction in *d* electrons, Phys. Rev. B **90**, 165108 (2014).

[60] C. Donnerer, X-ray studies of magnetic and structural transitions in iridates, Ph.D. dissertation, Department of Physics and Astronomy University College London, 2017.

[61] P. G. Klemens, Anharmonic decay of optical phonons, Phys. Rev. **148**, 845 (1966).

[62] C. Kant, J. Deisenhofer, T. Rudolf, F. Mayr, F. Schrettle, A. Loidl, V. Gnezdilov, D. Wulferding, P. Lemmens, and V. Tsurkan, Optical phonons, spin correlations, and spin-phonon coupling in the frustrated pyrochlore magnets $CdCr_2O_4$ and $ZnCr_2O_4$, Phys. Rev. B **80**, 214417 (2009).

[63] J. S. Lee, T. W. Noh, J. S. Bae, I.-S. Yang, T. Takeda, and R. Kanno, Strong spin-phonon coupling in the geometrically frustrated pyrochlore $Y_2Ru_2O_7$, Phys. Rev. B **69**, 214428 (2004).

[64] J. Laverdière, S. Jandl, A. A. Mukhin, V. Y. Ivanov, V. G. Ivanov, and M. N. Iliev, Spin-phonon coupling in orthorhombic $R\mathrm{MnO}_3$(R = Pr, Nd, Sm, Eu, Gd, Tb, Dy, Ho, Y): A Raman study, Phys. Rev. B **73**, 214301 (2006).

[65] T. M. H. Nguyen, L. J. Sandilands, C. H. Sohn, C. H. Kim, A. L. Wysocki, I.-S. Yang, S. J. Moon, J.-H. Ko, J. Yamaura, Z. Hiroi, and T. W. Noh, Two-magnon scattering in the 5*d* all-in-all-out pyrochlore magnet $Cd_2Os_2O_7$, Nat. Commun. **8**, 251 (2017).

[66] H. Kumar, V. Sathe, and A. Pramanik, Spin-phonon coupling in hole-doped pyrochlore iridates $Y_2(Ir_{1-x}Ru_x)_2O_7$: A Raman scattering study, J. Magn. Magn. Mater. **478**, 148 (2019).

[67] B. S. Araújo, A. M. Arévalo-López, C. C. Santos, J. P. Attfield, C. W. A. Paschoal, and A. P. Ayala, Spin–phonon coupling in monoclinic $BiCrO_3$, J. Appl. Phys. **127**, 114102 (2020).

[68] C. H. Sohn, C. H. Kim, L. J. Sandilands, N. T. M. Hien, S. Y. Kim, H. J. Park, K. W. Kim, S. J. Moon, J. Yamaura, Z. Hiroi, and T. W. Noh, Strong spin-phonon coupling mediated by single ion anisotropy in the all-in–all-out pyrochlore magnet $Cd_2Os_2O_7$, Phys. Rev. Lett. **118**, 117201 (2017).

[69] E. Granado, A. García, J. A. Sanjurjo, C. Rettori, I. Torriani, F. Prado, R. D. Sánchez, A. Caneiro, and S. B. Oseroff, Magnetic ordering effects in the Raman spectra of $La_{1-x}Mn_{1-x}O_3$, Phys. Rev. B **60**, 11879 (1999).

[70] Y. Xu, H. Man, N. Tang, T. Ohtsuki, S. Baidya, S. Nakatsuji, D. Vanderbilt, and N. Drichko, Phonon spectrum of $Pr_2Zr_2O_7$ and $Pr_2Ir_2O_7$ as evidence of coupling of the lattice with electronic and magnetic degrees of freedom, Phys. Rev. B **105**, 075137 (2022).